Response of cathodoluminescence to crystal-plastic deformation in zircon

Nicholas E. Timms* and Steven M. Reddy

n.timms@curtin.edu.au, s.reddy@curtin.edu.au

Dept of Applied Geology, Curtin University of Technology, GPO Box U1987, Perth, WA 6845, Australia

* Corresponding author.

fax: +61-8-9266-3153

Tel.:+61-8-9266-4372

Abstract

Geochemical and geochronological studies of zircon are commonly supplemented by cathodoluminescence (CL) imaging because it provides a means of recognizing different generations of zircon growth at high spatial resolution. Crystal-plastic deformation of zircon can have significant effects on zircon geochemistry. Detailed analyses from electron backscatter diffraction mapping combined with panchromatic CL imaging and hyperspectral CL mapping of several crystal-plastically deformed grains from different geological settings are used to establish the relationships between crystal-plastic deformation and CL in zircon. Results show a strong spatial association between deformation microstructures and CL response that lead to modification of CL that commonly cross-cuts primary zoning. Variable contributions from two fundamental deformation-related processes result in a variety of CL characteristics: A defect control on panchromatic CL intensity, particularly at low-angle (subgrain) boundaries; and changes in spectral CL response due to deformation-related modification of CL-active REE geochemistry. A framework is provided for the recognition of deformation-related microstructures using CL and the usefulness of CL imaging in the discrimination of these microstructures is critically evaluated.

Key Words: Cathodoluminescence, EBSD, microstructure, zircon, REE, deformation

1. Introduction

Panchromatic cathodoluminescence (PCL) imaging commonly supplements a range of studies of zircon ($ZrSiO_4$) because it is a rapid, high-spatial resolution means of recognizing fine scale intragrain growth zoning and recrystallisation textures, and provides a framework for the interpretation of geochronological and geochemical analyses (Corfu et al., 2003; Geisler et al., 2003; Hanchar and Miller, 1993; Hanchar and Rudnick, 1995; Hoskin, 2000; Hoskin and Black, 2000; Pidgeon, 1992; Vavra, 1990). The phenomenon of CL in crystalline solids is caused by the emission of radiation as electrons excited by external irradiation (such as visible light or an electron beam) return to their lower energy ground states. Cathodoluminescence in minerals is typically activated by substitutional trace elements with equivalent valence states at specific sites in the crystal lattice (Pagel et al., 2000). Many of the factors that contribute to the CL signal of zircon are well established. Studies of natural and synthetic zircon show that the presence of various CL-active impurity ions, such as trivalent rare earth elements (REE^{3+}), causes narrow luminescence emission peaks at characteristic wavelengths (Table 1) (Blanc, 2000; Cesbron et al., 1995; Nasdala et al., 2002; Nasdala et al., 2003; Remond et al., 1992). In natural zircon, narrow REE peaks are commonly superimposed on a broad emission peak (Table 1). The origin of so-called ‘broadband’ CL is not well understood and has been attributed to point defects (Koschek, 1993), OH- defects (Remond et al., 1992), or defects within the silica tetrahedra (Kempe et al., 2000). The sum of all of the luminescence bands gives the integrated intensity seen in panchromatic CL images.

Crystal defects, such as structural disorder associated with radiation damage, have been shown to suppress CL intensity in zircon (Geisler and Pidgeon, 2001; Nasdala et

al., 2002), because the presence of crystal defects proximal to CL-activator elements changes the crystal field symmetries and can lead to non-luminescence (Geisler and Pidgeon, 2001; Geisler et al., 2001).

Recent studies show that zircon can deform by crystal-plasticity at crustal conditions (Reddy et al., 2007) and that deformation-related microstructures and/or associated chemical changes may modify CL signal (Reddy et al., 2007; Reddy et al., 2006; Timms et al., 2006). However, the relationships between CL and deformation-related microstructures are not well documented and remain poorly understood. This paper utilizes panchromatic CL imaging and hyperspectral CL mapping of several examples of deformed zircon grains from different geological settings to characterize the range of responses to crystal-plastic deformation. In so doing the potential use of CL imaging for the reliable identification of plastic deformation is assessed. This is the first detailed study of the effects of deformation on the CL characteristics of zircon.

2. Sample characteristics

Five zircon grains were selected to illustrate a variety of effects of different styles of crystal-plastic deformation on zircon CL response. Three grains come from ultramafic and mafic rocks including an Archaean pyroxenite from NW Scotland (GST15), an Indian Ocean gabbroic mylonite (IOZ), and a mantle xenolith from the Udachnaya kimberlite, Siberia (UX), and two grains are from an undeformed andesite from Java (Fig. 1; Table 2). The general paucity of zircons in pyroxenites, mantle xenoliths and mafic rocks means that, when present, they can provide important constraints on geological processes and increased emphasis is placed on geochronological and geochemical data from these grains. Therefore, it is critical to be able to identify and

84 interpret deformation microstructures and their CL response to correctly interpret
85 geochronological and geochemical information from such samples.
86 Sample GST15 is one of several large (c.12.5 mm long), subhedral, deformed zircon
87 grains from the margin of a syntectonic pyroxenite intrusion (Kinny and Friend, 1997)
88 (Fig. 1a). The grain was crystal-plastically deformed soon after crystallization,
89 probably during regional amphibolite-facies Inverian metamorphism (Timms et al.,
90 2006). IOZ is a single magmatic zircon hosted in a deformed gabbro recovered from
91 Ocean Drilling Program Leg 735B drilled at the Atlantis II slow spreading ridge in the
92 Indian Ocean (Dick et al., 2000). The grain is within a 1cm-wide amphibolite-facies
93 shear zone predominantly composed of recrystallised plagioclase and magnetite
94 (Reddy et al., 2007) (Fig. 1b). Grain UX is an anhedral zircon, the largest (>900μm
95 long) grain in a zircon-rich zone of a partially metasomatised garnet websterite mantle
96 xenolith (U2268) from the Udachnaya kimberlite, Siberia (Fig. 1c). Udachnaya
97 peridotite xenoliths preserve assemblages with a range of mantle PT conditions from
98 750-1380°C and ~75-210 km depth, (Boyd et al., 1997). The grains from ultramafic
99 and mafic rocks were originally selected for study for their large size allowing
100 multiple in-situ ion probe analyses to facilitate quantitative comparison with
101 deformation microstructures, which is not presented here.
102 The two grains from an undeformed, Miocene porphyritic andesite from the Ponorogo
103 district of East Java (sample Jhs2PON4 of Smyth et al. (2007)), are more akin to
104 zircon routinely analysed for geochronology and/or geochemistry. Two grains are
105 from a population of euhedral magmatic zircon grains with a weighted mean
106 $^{207}Pb/^{206}Pb$ crystallisation age of 9.3 ± 0.2 Ma (Reddy et al., 2008b). Approximately
107 80% of the population preserve crystal-plastic deformation microstructures, and the
108 grains (5 and 8 of Reddy et al. (2008b)) are representative of the style of deformation

found in the zircon. The host rock contains plagioclase and hornblende phenocrysts and glomerocrysts in a fine groundmass. Deformation of the zircons occurred within a magma chamber during a low melt fraction cumulate stage before later disaggregation by melt rejuvenation (Reddy et al., 2008b).

3. Analytical Procedure

Zircon grains from GST15 and Jhs2PON4 were separated from crushed rock samples using magnetic and methylene iodide liquid separation, then mounted in epoxy resin and polished to approximately half their thickness. For samples IOZ and UX, petrographic thin sections were progressively polished down to 0.25μm diamond paste. All of the samples were given a further polish with 0.06μm colloidal silica NaOH suspension (pH 9.8) on a Buehler Vibromet II polisher. Colloidal silica polishing times varied between samples from 2-6 hours. A carbon coat was applied prior to CL imaging. For EBSD analysis, previous coats were removed by further polishing (<30 minutes) with colloidal silica, and a light C-coat (c. 2 nm thick) was applied to reduce the effects of charging under the electron beam but maintain a strong EBSD signal. EBSD map data were collected using the SEM facilities at the Microstructural Analysis Facility, Curtin University, part of the Nano-scale Characterization Centre, WA, except EBSD mapping of IOZ which was collected using a Philips XL30 FEG SEM at the University of Adelaide, South Australia. EBSD data were acquired using a Nordlys 1 detector with 20kV accelerating voltage, 20mm working distance, spot size ~0.5μm, and tilt of 70°. Settings for electron backscatter pattern (EBSP) collection are given in Table 3 following Reddy et al. (2008a). EBSPs were indexed to theoretical reflector files generated via Channel 5 Twist software

using structural data for zircon that include Oxford Instruments (HKL Technology Ltd.) “Best in Family” default zircon phase, and zircon at 1 atmosphere and 9.8 GPa from Hazen and Finger (1979), equivalent to zircon [2] and zircon [3] from the Mincryst crystallographic database (Chichagov et al., 2001; Reddy et al., 2008a) (Table 3). All EBSD data were processed using Oxford Instruments Channel 5.9 software with a variety of settings and parameters (Table 3). The raw EBSD data were processed using the noise reduction procedure described by Reddy et al. (2007) (Table 3). Visual comparison of the processed data with original data shows that no significant artefacts were generated through noise reduction. Misorientation analysis involves determination of the angle/axis pair that describes the minimum misorientation between two differently oriented structures (Wheeler et al., 2001). Minimum misorientation is commonly referred to in materials science literature as ‘disorientation’ and is referred to herein simply as ‘misorientation’. Cumulative misorientation maps were generated by colouring each pixel for misorientation from a user-defined reference orientation of the grain, and show absolute orientation variations within a grain (Reddy et al., 2008b). The boundaries between adjacent data points with different misorientation angles (0.5-1˚, 1-2˚, >2˚) were plotted as solid lines, superimposed on cumulative misorientation maps, to show the orientation boundary microstructure. Misorientation axis maps were produced by colour assignment to low-angle (>0.5˚) boundaries for their misorientation axis orientation within the (user defined) sample x-y-z reference frame. In these maps, adjacent subgrains that have misorientation axes parallel to x, y, or z have red, green or blue boundaries, respectively. A constant colour along the length of a boundary indicates consistency in the axis geometry.

Panchromatic CL images were collected using a CCD-Si collector mounted on a Philips XL30 SEM at Curtin University of Technology with 10kV accelerating voltage, spot size of ~0.5μm and 15mm working distance. Hyperspectral CL maps of each grain were acquired by automated collection of CL spectra at nodes on a user-defined grid using a 2049-element linear spectrometer/CCD-Si mounted on a Jeol JXA8200 microprobe at the Advanced Analytical Centre, James Cook University, Townsville, Australia. The accelerating voltage was 20kV, with the minimum spot size (~1μm) and 100nA probe current. Instrument sensitivity is 86 photons/count and has a spectral range of 331.4 to 1826.9 nm. A grating of 300 lines/mm and blaze width of 500 nm were used. The setting details for individual maps are given in Table 3. Trichromatic CL maps were produced from wavelength CL data by assignment of narrow wavelength ranges to three colour channels. Spectral windows at 390-410, 540-560 and 595-620 nm encompass common dominant peaks for Er^{3+}, Tb^{3+} and Eu^{3+} plus Sm^{3+} in zircon, respectively, and have been chosen to highlight relative changes in HREE through MREE. The data were managed through XCLent operating software (MacRae et al., 2005).

4. Results

4.1 Microstructure Characteristics

All of the samples analysed in this study preserve microstructures with similar characteristics that include orientation variations accommodated by a combination of both progressive bending of the lattice and discrete (<1μm wide) low-angle (generally <10˚) boundaries (Figs 2-6). These microstructures are commonly heterogeneously distributed across each grain, and not limited to the grain margins. The total

cumulative misorientation varies across each grain from ~10˚ (Fig. 5a) to ~23˚ (Fig. 6c). The most misoriented domains in the Jhs2PON4 grains are within the grain interior, whereas they are generally towards the grain edge in the other examples. Detailed accounts of the microstructural characteristics of GST15 and IOZ are given by Timms et al., (2006) and Reddy et al. (2007) respectively, and are summarized briefly here.

The appearance and geometry of low-angle boundary microstructure also varies from sample to sample (Figs 2b, 4b, 5b, 6e, f). Boundaries in IOZ are sub-parallel and form deformation 'bands', whereas boundaries in the other samples form polygonal networks that subdivide the zircon into 'subgrains' with relatively consistent internal orientations (e.g., Figs 2a, 3, 5b, 6c, d). The size of orientation sub-domains is variable within and between individual samples, and is typically 5-150 μm. In all cases, a hierarchy of orientation boundaries is present with numerous boundaries that accommodate low misorientation angles (<1.5˚) and comparatively few higher-angle (<10˚) boundaries (Fig. 7). Where low-angle boundaries do not intersect other boundaries or the grain edge, they dissipate into wider domains of orientation variation.

Stereographic analysis of crystallographic pole orientations for each data point of the EBSD maps shows gradual, cumulative dispersion of crystallographic axes that are consistent with the orientation variations shown by the cumulative misorientation maps. IOZ shows a simple dispersion about a single <100> direction (Fig. 8b). GST 15, UX and grain 8 from Jhs2PON4 show complex dispersion patterns that are dominated by combinations of <001> and <100> rotation axes (Fig 8a, c, e), whereas

206 the dispersion of crystallographic poles in grain 5 from Jhs2PON4 is dominated by a
207 single rotation about the <001> direction (Fig.8d). The misorientation axes describing
208 the geometrical coincidence between adjacent data points are systematically aligned
209 in similar orientations to the dominant rotation axes that account for the
210 crystallographic dispersion patterns (Fig. 8). Importantly, additional clusters of
211 misorientation axes are identifiable for samples that show complex dispersion
212 patterns. In most cases, these minor populations of axes are also parallel with low-
213 index directions. For example, two discrete minor clusters of 2-4˚ data in GST15 align
214 with {111} and {011} poles respectively (Fig. 8bi) and correspond with two different
215 low-angle boundaries (Fig. 2b). In UX, 2-5˚ misorientation axes cluster at or near
216 {100} poles, whereas 1-2˚ misorientation axes form several clusters that align with
217 higher-index directions in zircon, and tend to be aligned along the {001} and {010}
218 planes (Fig. 8c). The two Jhs2PON4 grains show systematic alignment of higher-
219 angle misorientation axes with low-index directions, and a minor component of 1-5˚
220 misorientation axes clustering at higher-index positions (Fig. 8d-e).
221

222 **4.2 Cathodoluminescence**

223 Each grain has different CL characteristics in both panchromatic CL images and
224 wavelength CL maps (Figs 2c,d, 4c, d, 5c, d, 6g, j). The GST15 grain is largely
225 uniform with no oscillatory zoning in panchromatic CL, with a broad decrease in CL-
226 intensity toward the grain edge (Fig. 2c, 3b). This pattern is disrupted by a complex
227 network of CL-dark bands (Figs 2c, 3b). Typically, the borders of the dark CL bands
228 are diffuse, with CL gradients away from the bands, and the bands tend to terminate
229 into broader dark CL areas where they do not link with other bands (Figs 2c, 3b).
230 Narrow (up to 20μm wide) zones of bright CL sharp edges transect the grain and cut

231 across the network of dark CL signal and probably represent healed fractures. The
232 network of dark CL bands and bright CL domains is cut by sets of brittle fractures.
233 Hyperspectral CL mapping shows that the CL signal of the centre of the host 'low
234 strain' zircon is dominated by a broad peak centred at ~550 nm with minor peaks at
235 ~500 and ~600 nm (Fig. 9b). The spectral variations that define the dark bands are
236 caused by panchromatic reduction of CL emission without shifts in the relative
237 intensity of different peaks (Fig. 9b).
238
239 Panchromatic CL imaging of IOZ shows fine-scale oscillatory growth zoning
240 characteristic of igneous zircon (Fig. 4c). The CL intensity contrast between the
241 oscillatory bands is reduced in the deformed region of the grain such that the strong
242 zoning is replaced by mid grey CL emission where the zoning is barely visible. This is
243 overprinted by discrete, narrow (~1μm) darker bands that are oblique to oscillatory
244 growth zoning (Fig. 4c). Hyperspectral CL data reveals that the region with reduced
245 contrast in oscillatory zoning corresponds to a shift in the wavelength characteristics
246 of CL emission. Spectral analysis of the grain centre shows a broad peak centred at
247 ~400nm with minor peaks superimposed at ~420nm, ~470nm, ~550nm and ~600nm
248 (Figs 4d, 9a). In comparison, CL spectra from the reduced contrast domain show a
249 similar general form but with decreased luminescence at ~400nm and ~470nm, and
250 increased intensity of peaks at ~550nm and ~600nm.
251
252 The UX grain does not show oscillatory or sector zoning in panchromatic CL, and
253 heterogeneously developed CL-dark bands cross-cut a uniform CL pattern (Fig. 5d).
254 UX has a broad spectral peak centred at ~470nm with superimposed fine structure at
255 ~430, 500, 550 and 600 nm (Fig. 9c). The CL spectra from the dark bands have peaks

at the same wavelengths with the same relative magnitudes as the adjacent domains, and differ only in panchromatic intensity (Figs 5d, 9c). This CL texture is disrupted by very subtle, discrete linear features (up to a few microns wide) revealed by wavelength CL that commonly track along the dark bands, and in other places transect the microstructure (Fig. 5d). Spectral analysis shows that the CL-bright features are caused by a decrease in the 475 nm peak and a relative increase in peak intensities at ~550 nm and ~605 nm.

The zircon grains from Jhs2PON4 have euhedral, bright CL cores with strongly oscillatory zoned rims in panchromatic CL (Fig. 6g-h). The cores are not oscillatory zoned and contain diffuse curvilinear substructures that do not continue into the rims. Localized disruption of the CL pattern in the cores and rims is visible in panchromatic CL. Blocks of rotated and distorted zoning rimmed by dark CL boundaries coincide with the position of sub-domains bound by orientation boundaries identified by EBSD (Fig. 6). The CL spectra of Jhs2PON4 grains are dominated by a broad, asymmetric peak centred at ~400 nm, with narrow minor peaks superimposed on the long wavelength tail at ~500, ~550 and ~605 nm (Fig. 9d-e). CL contrast of primary oscillatory zoning in the undisturbed parts of the grain is generated by panchromatic CL intensity variations rather than shifts in the spectral response. Hyperspectral CL mapping reveals that discrete domains of high local misorientation that cross-cut the primary growth zoning locally show a significant spectral shift with a relative increase of the 500, 550 and 605 nm peaks over peaks at lower wavelengths (Figs 6g-h, 9d-e).

5. Discussion

5.1 Explanation of Orientation Variations

In all samples, the orientation variations identified by EBSD mapping are accommodated by a combination of progressive orientation change and discrete low angle boundaries, most commonly with systematic low-index crystallographic relationships. These microstructures do not have surface topographic expression and do not correspond to visible fractures identified using optical microscopy (with the exception of a complex zone in GST 15 shown in Fig. 2). These characteristics are consistent with the formation and migration of dislocations through the crystal structure, i.e., dislocation creep and subsequent recovery (Reddy et al., 2007; Reddy et al., 2006; Timms et al., 2006), rather than by brittle fracture (Boullier, 1980; Rimsa et al., 2007; Steyrer and Sturm, 2002) or solid-state recrystallisation (Hoskin and Black, 2000). The data show that crystal-plastic deformation microstructures can affect significant areas of the grains and are not always located at the tips or localized at the grain margins.

Low-angle boundaries are formed during dislocation creep by the accumulation of dislocations into boundary planes to accommodate the progressive bending of a crystal lattice and minimise defect energy of the lattice, and their geometry is a direct consequence of the geometry of contributory slip system(s) (Boyle et al., 1998; Lloyd et al., 1997; Prior et al., 2002). This allows the slip system associated with a particular dislocation geometry to be determined by utilizing a simple geometric model that relates the low-angle boundary orientation and misorientation axis to the Burgers vector and slip plane (Prior et al., 2002; Reddy et al., 2007). The analysis of misorientation axes and low-angle boundary geometry shows that zircon grains

contain a variety of dislocation geometries, which indicate that zircon can deform by several slip systems, even within a single grain. Analysis of the grains indicates the operation of the two main slip systems <100> {001} and <001> {100} (and symmetric equivalents), both of which are known slip systems for zircon (Leroux et al., 1999; Reddy et al., 2007; Timms et al., 2006). Boundaries with misorientation axes that coincide with higher index directions, such as <011> and <111> in GST15, or <012> in Jhs2PON4 grain 5, are less common and are a consequence of higher index slip systems, or a result of combinations of different slip systems at a scale that cannot be resolved by the EBSD data (Reddy et al., 2007).

5.2 The effects of crystal-plastic deformation on cathodoluminescence in zircon

5.2.1 Spatial relationship between deformation microstructure and CL textures

In all of the studied samples the effects of crystal-plastic deformation is reflected in CL, with textures that cross cut, disrupt and/or overprint primary growth features. However, the exact response of CL to crystal-plastic deformation is varied, and attributed to two phenomenon – panchromatic reduction in CL response and spectral shifts in the CL response. Additional complexity can be seen in GST15 where new, CL-bright zircon has grown along a domain of crystal-plastic and brittle deformation, either by solid state recystallisation driven by lattice strain energy, or growth into open fracture porosity (Fig. 2).

5.2.2 Panchromatic reduction in CL response – the effect of structural defects

The localized low-luminosity domains associated with low-angle boundaries are interpreted to result from secondary modification of CL due to crystal-plastic processes. The presence of discrete low-angle boundaries implies that the adjacent

329 crystal volume has been swept by a population of dislocations. At high temperatures
330 where this process is efficient, these volumes have a relatively low dislocation
331 density, whereas low-angle boundaries have a significantly higher ’geometrically
332 necessary’ dislocation density. The accumulation of dislocations into low-angle
333 boundaries lowers the strain energy of the surrounding crystal volume. Localised loss
334 of CL response at low-angle boundaries suggests that high dislocation densities within
335 low-angle boundary regions has led to short range disorder and disruption of CL-
336 active impurity site symmetry. Both of these factors have been proposed to
337 significantly affect CL in ‘undeformed’ zircon (Blanc, 2000; Cesbron et al., 1995;
338 Geisler and Pidgeon, 2001). Boundary misorientation angle seems to have a greater
339 effect on loss of CL response than specific slip system geometry, with the darkest
340 domains corresponding with the highest angle boundaries (Fig. 3).
341 The pattern of progressive reduction of panchromatic CL signal developed broadly
342 around low-angle boundaries in GST15 and UX suggests that the migration of
343 dislocations into low-angle boundaries was not efficient. In contrast, the JhsPON4
344 grains tend to have sharply localized reduction in CL response at low-angle
345 boundaries, and IOZ shows virtually no low-angle boundary effect, perhaps as a
346 consequence of efficient dislocation glide and climb (Fig 3). Asymmetrically
347 developed patterns of reduced panchromatic CL is observed around some of the low-
348 angle boundaries in GST15 and UX and could reflect low-angle boundary mobility,
349 where zircon with modified CL response occurs in the trail behind advancing
350 boundaries (Figs 2, 3, 5). Alternatively, this pattern could be a consequence of beam
351 interaction with low-angle boundaries at shallow angles to the polished surface, in
352 agreement with escape depth (activation volume) of CL which is generally

353 significantly larger than for EBSD, secondary and backscattered electrons (Kempe et
354 al., 2000; Nasdala et al., 2004).
355
356 Timms et al. (2006) demonstrated that enrichment of U and Th can occur at low-angle
357 boundaries due to the creation of enhanced-diffusivity pathways. Although the
358 presence of U and Th does not cause CL loss, the accumulated microstructural
359 damage due to α-decay over time could locally suppress panchromatic CL intensity.
360 However, the maximum accumulated α-doses calculated for the young and U-Th poor
361 zircon in this study are low, even for the most U- and Th-enriched domains in GST 15
362 (6.53×10^8 events/mg, after Murakami et al. (1991)) and are unlikely to have
363 suppressed CL. Radiation damage related loss of CL response in other deformed
364 samples depends on factors such as the concentration of U and Th, timing of
365 enrichment, the thermal (annealing) history of the zircon.
366
367 ***5.2.3 Spectral shifts in CL signal – geochemical effects***
368 Hyperspectral CL mapping shows narrow emission peaks at known wavelengths for
369 REE^{3+} suggesting that these and other CL-active trace elements are present in the
370 analyzed samples. Detectable peaks correspond to the following CL-active REE^{3+} in
371 each sample: Er^{3+}, Dy^{3+}, Tb^{3+}, Sm^{3+} Eu^{3+} in IOZ and UX; Dy^{3+}, Tb^{3+}, Sm^{3+} Eu^{3+} in
372 GST15; and Er^{3+}, Tb^{3+}, Sm^{3+} Eu^{3+} in the Jhs2PON4 grains. Localized differences in
373 CL emission wavelengths associated with crystal-plastic deformation microstructures
374 occur in all except one sample. A change in the relative intensity of REE^{3+} emission
375 peaks is interpreted to reflect changes in the relative concentration of different CL-
376 active REE^{3+}. This interpretation has been verified by quantitative ion microprobe
377 analysis of IOZ which records a bulk increase in all REE^{3+}, and a preferential increase

in middle over heavy REE^{3+} with deformation (Reddy et al., 2006). However, calibration of CL spectra to quantify ionic concentrations is not possible due to non-unique solutions for the deconvolution of CL spectra, primarily arising from interference from different peaks, unknown orientation effects, the competing effect of structural integrity, and instrumental factors such as spectrometer response corrections. Even so, a similar pattern of relative intensification of middle REE^{3+} peaks (e.g., Sm^{3+}, Eu^{3+}, Tb^{3+}) over heavy REE^{3+} (e.g., Er^{3+}) implies middle REE enrichment in deformed zones in all except one example, and indicates that wavelength modification could be a common phenomenon that accompanies crystal-plastic deformation (Fig. 9). Such changes in zircon composition are best explained by enhanced diffusion associated with the development of crystal-plastic deformation microstructures. Reddy et al. (2006) report REE diffusion distances associated with crystal-plastic high diffusivity pathways in IOZ that are 10^5 greater than those expected from experimentally-derived, volume diffusion parameters (Cherniak et al., 1997). The spatial extent to which REE composition has been modified is shown by the trichromatic wavelength CL maps and varies between the samples (Figs 1, 3-5). In IOZ, the modified domain encompasses all of the deformed area and is not limited to low-angle boundaries. In contrast, REE modification in Jhs2PON4 grains is restricted to low-angle boundaries and domains of high local misorientation. In UX, REE enrichment is most pronounced along the low-angle boundary network, with additional patchy modification in the deformed domain that is not related to the current position of low-angle boundaries.

Although the results of this study suggest that deformation-related REE modification could be a common process, little is known about the diffusion characteristics of

crystal-plastic deformation microstructures in zircon. The enrichment of middle over heavy REEs in modified zircon could be a product of the chemical reservoir for exchange and/or differences in diffusivity between REEs due to ionic radii variations in a similar way to empirically derived diffusion parameters (e.g., the activation energy, E, and diffusion coefficient, D_0) for volume diffusion (Cherniak et al., 1997). Deformation-related REE enrichment of zircon implies interaction with a REE source, such as a REE bearing fluid, and light REE enrichment or depletion depends on the stability of REE-bearing phases and the grain boundary fluid chemistry (e.g., Rolland et al., 2003).

5.3 Evaluation of CL imaging for detecting and interpreting deformation microstructures

The net effect of deformation and related processes on the finite CL texture will be governed by the interaction between rates of dislocation glide and climb, recovery, pathway diffusivity (dynamic and arrested), intrinsic defect structure, impurity source availability, and temperature-time history. The resultant texture may be uncomplicated (e.g., IOZ) or have complex overprinting relationships (e.g., UX). Some of the examples in this study illustrate that deformation-related microstructures can be clearly identified in cathodoluminescence images, such as in UX and GST15 where there is no primary growth zoning, or where primary growth zoning is clearly disrupted, such as for grain 5 of Jhs2PON4. However, other samples show that deformation microstructures can be cryptic. This is true where deformation has resulted in changes in emission wavelength but with negligible changes to the integrated emission intensity. In other cases, primary CL features may dominate and

deformation effects on panchromatic CL images can be very subtle and easily overlooked.

A current analytical problem is that crystal-plastic deformation microstructures can cause geochemical heterogeneity at finer scales than the spatial resolution of many current quantitative microbeam techniques, such as ion microprobe and laser ICP-MS. This study illustrates that wavelength CL mapping can be a useful technique to spatially resolve variations in REE in zircon semi-quantitatively, and down to ppm levels, at the same scale as microstructural analysis by EBSD. However, interplay between various controls on CL leads to ambiguities associated with the interpretation of panchromatic CL images and hyperspectral CL maps. Given that deformation can be accompanied by geochemical modification of zircon, and that deformation-related textures are not always clear on CL images, it is important to identify and characterize deformation in zircon via other imaging techniques, such as orientation contrast imaging, or orientation mapping by electron backscatter diffraction. In conclusion, this study highlights that CL imaging and orientation mapping can be a powerful combination for robust interpretations of intragrain characteristics of zircon.

6. Acknowledgements

We are honoured to have the opportunity to contribute to this special tribute issue to Bob Pidgeon – an early pioneer in the interpretation of catholuminescence textures in zircon. We acknowledge an Australian Research Council Discovery Grant (DP0664078) and a Curtin University Targeted Research Fellowship (Reddy) that provided funding to undertake this research. Pat Trimby, Pete Kinny, and Joseph Hamilton are thanked for supplying the various zircon samples used in this study. We are grateful to Kevin Blake at the Advanced Analytical Centre, Townsville, for assistance in collection of hyperspectral CL maps. Thorsten Geisler and an anonymous reviewer are thanked for their comments that led to improvements in the final manuscript. Thanks to Simon Wilde for editorial handling. This is TIGeR publication number 126.

Figure 1

Photomicrographs and maps of the samples utilized in this study. (ai) Reflected light optical image of zircon-bearing pyroxenite GST15. (aii) Cumulative misorientation map and profile of zircon grain from GST15. (b) Backscatter electron image of IOZ. (ci) Optical micrographs of mantle xenolith U2268 showing the context of zircon UX. (cii) Detail of area shown in (ci). (d) Panchromatic CL image of magmatic zircon population separated from Jhs2PON4 (after Reddy et al. (2008b)). 80% of the grains preserve crystal-plastic deformation microstructures (indicated by dots).

Figure 2

(a) Cumulative orientation map, (b) boundary misorientation axis geometry map, (c) panchromatic CL image, and (d) hyperspectral CL map of the deformed tip of the zircon grain from GST15 (after Timms et al. (2006)). The microstructure is dominated by a complex pattern of orientation domains with <5˚ misorientation boundaries that cumulatively accommodate ~11˚ of misorientation across the area shown. Orientation boundaries in (a) form a polygonal network and are sites of lower panchromatic CL intensity in (c) than the orientation domains. The complex zone shown in lower left contains a combination of ductile and brittle deformation microstructures, and contains patches of recrystallised bright-CL zircon. (b) shows systematic geometric relationships between misorientation axes and differently oriented boundaries. The colour uniformity in (d) indicates no relative changes in Er^{3+}, Tb^{3+}, Sm^{3+} or Eu^{3+} peak intensities. Profile (i) to (ii) and boundary labelled α shown in Fig. 3. Dark ellipses in (a) and (b) are non-indexed points over ion probe analysis pits. Boundary β shows asymmetrically developed pattern of reduced-CL. Refer to text and Fig. 8 for

484 explanation of crystallographic direction annotations in (b). Numbered areas in (d)
485 correspond to CL spectra shown in Fig. 9.
486
487 Figure 3
488 (a) Misorientation profile and (b) panchromatic CL intensity profiles for transect (i) to
489 (ii) shown in Fig. 2. Peaks in the non-cumulative misorientation profile correspond to
490 low-angle boundaries. (b) shows a general, gradual decrease in CL intensity from left
491 to right with negative excursions that generally correspond to the position of low-
492 angle boundaries. Range bars indicate the approximate extent of significant CL-
493 quenching associated with >0.5˚ boundaries. Note the asymmetry of profile associated
494 with boundary labelled α. See text for discussion.
495
496 Figure 4
497 (a) Cumulative orientation map, (b) boundary misorientation axis geometry map, (c)
498 panchromatic CL image, and (d) hyperspectral CL map of the deformed tip of IOZ
499 (after Reddy et al. (2006)). The grain records 14˚ of cumulative lattice strain
500 accommodated by sub-parallel low-angle boundaries. Oscillatory CL growth zones
501 are homogenized in the deformed region. Arrows in (b) highlight selected boundaries
502 visible in (c). Arrows in (c) highlight linear dark bands that correspond to low-angle
503 boundaries. Colour change from blue-green to red in (d) indicates increase in the REE
504 CL peak for Tb^{3+} relative to Er^{3+}. Numbered areas in (d) correspond to CL spectra
505 shown in Fig. 9b.
506
507 Figure 5

(a) Cumulative orientation map, (b) boundary misorientation axis geometry map, (c) panchromatic CL image, and (d) hyperspectral CL map of the deformed tip of UX. The grain records a cumulative misorientation of up to 10˚ towards the corners of the grain, accommodated by a system of well-defined 1-5˚ boundaries and less discrete <1˚ boundaries. (b) shows systematic geometric relationships between boundary orientation and boundary misorientation axes. (bi) indicates a domain of distributed lattice strain, (bii) indicates a discrete low-angle boundary. (c) shows patchy domains of featureless panchromatic CL disrupted by variably low-luminescent domains that mimic the deformation microstructure. (d) shows an additional complexity of distinctive yellow patches and ribbons that indicate increased luminescence from Tb^{3+}, Sm^{3+} and Eu^{3+} relative to Er^{3+}. Numbered areas in (d) correspond to CL spectra shown in Fig. 9c.

Figure 6

(a-b) Cumulative orientation maps, (c-d) boundary misorientation axis geometry maps, (e-f) panchromatic CL images, (g-h) hyperspectral CL maps of grains 5 and 8 from Jhs2PON4 (Fig. 1d). (a-b) show that both grains preserve heterogeneously distributed polygonal orientation sub-domains, particularly on their flanks. These are separated by low-angle (<5˚) boundaries with systematic misorientation axes (c-d) that accommodate cumulative misorientation of 23˚ and 12 ˚ across grains 5 and 8, respectively. See text for description of (e) to (h). Numbered areas in (g-h) correspond to CL spectra shown in Fig. 9d, e. ((d, b, e and f) after Reddy et al. (2008b)).

Figure 7

Distribution of correlated (i.e., for adjacent data points) misorientation angles for (a) GST15, (b) IOZ, (c) UX, and (d-e) grains 5 and 8 from Jhs2PON4. Each grain contains a high relative frequency of low misorientation angles and a progressively lower proportion to higher misorientation angles. See text for discussion.

Figure 8

Stereographic projections of crystallographic data from EBSD maps on Figs 2, 4-6 for (a) GST15, after Timms et al. (2006), (b) IOZ, (c) UX, and (d-e) grains 5 and 8 from Jhs2PON4, respectively. (i) Pole to selected low-index planes for all data on each map. Colours correspond to misorientation away from a reference orientation as shown in previous figures. (ii) Plots of 0.5-5˚ misorientation axis data for adjacent EBSD analysis points. (a.i) Data is a subset that does not include misorientation axes that relate to late brittle fractures. (i) and (ii) plotted as lower hemisphere equal area projections in the user-defined sample x-y-z coordinate system.

Figure 9

Selected CL emission spectra from (a) GST15 (after Timms et al. (2006)), (b) IOZ, (c) UX, (d) Jhs2PON4 grain 5, and (e) Jhs2PON4 grain 8. Individual spectra represent the mean from approximately 10 by 10 μm areas corresponding to numbered points shown on hyperspectral CL maps in previous figures. Annotations include the position of the dominant peaks for REE^{3+}, and the wavelengths assigned to blue, green and red colour channels in wavelength maps in previous figures. See text for discussion.

7. References

Blanc, P., Baumer, A, Cesbron, F, Ohnenstetter, D, Panczer, G, Rémond, G, 2000. Systematic Cathodoluminescence Spectral Analysis of Synthetic Doped Minerals: Anhydrite, Apatite, Calcite, Fluorite, Scheelite and Zircon. In: M. Pagel, V. Barbin, P. Blanc and D. Ohnenstetter (Editors), Cathodoluminescence in Geosciences. Springer-Verlag, Berlin, pp. 127-160.

Boullier, A.M., 1980. A preliminary study on the behaviour of brittle minerals in a ductile matrix: example of zircons and feldspars. Journal of Structural Geology, 2: 211-217.

Boyd, F.R. et al., 1997. Composition of the Siberian cratonic mantle: evidence from Udachnaya peridotite xenoliths. Contributions to Mineralogy and Petrology, 128(2): 228-246.

Boyle, A.P., Prior, D.J., Banham, M.H. and Timms, N.E., 1998. Plastic deformatrion of metamorphic pyrite: new evidence from electron backscatter diffraction and forescatter orientation-contrast imaging. Mineralium Deposita.

Cesbron, F., Blanc, P., Ohnenstetter, D. and Rémond, G., 1995. Cathodoluminescence of rare earth doped zircons: I. Their possible use as reference materials. Scanning Microscopy Supplement, 9: 35-56.

Cherniak, D.J., Hanchar, J.M. and E.B., W., 1997. Rare-earth diffusion in zircon. Chemical Geology, 134: 289-301.

Chichagov, A.V. et al., 2001. MINCRYST: a Crystallographic Database for Minerals, Local and Network (WWW) Versions. Crystallography Reports, 46: 876-879.

Corfu, F., Hanchar, J.M., Hoskin, P.W.O. and Kinny, P., 2003. Atlas of Zircon Textures. In: J.M. Hanchar and P.W.O. Hoskin (Editors), Reviews in Mineralogy and Geochemistry: Zircon. Mineralogical Society of America, pp. 469-500.

Dick, H.J.B. et al., 2000. A long in situ section of the lower ocean crust: Results of ODP Leg 176 drilling at the Southwest Indian Ridge. Earth and Planetary Science Letters, 179(1): 31-51.

Gaft, M. et al., 2000a. Unexpected luminescence of Cr5+ and Cr3+ ions in ZrSiO4 zircon crystals. Journal of Luminescence., 87-89: 1118-1121.

590 Gaft, M., Panczer, G., Reisfeld, R. and Shinno, I., 2000b. Laser-induced luminescence of
591 rare-earth elements in natural zircon. Journal of Alloys and Compounds, 300-301:
592 267-274.

593

594

595 **Geisler, T. and Pidgeon, R.T., 2001. Significance of radiation damage on the integral**
596 **SEM cathodoluminescence intensity of zircon: an experimental annealing study.**
597 **Neues Jahrbuch Fur Mineralogie-Monatshefte, 2001(10): 433-445.**

598 **Geisler, T., Pidgeon, R.T., Van Bronswijk, W. and Pleysier, R., 2001. Kinetics of**
599 **thermal recovery and recrystallization of partially metamict zircon: a Raman**
600 **spectroscopic study. European Journal of Mineralogy, 13(6): 1163-1176.**

601 **Geisler, T., Schleicher, H., Pidgeon, R.T., Kurtz, R. and van Bronswijk, W., 2003.**
602 **Experimental hydrothermal alteration of partially metamict zircon. American**
603 **Mineralogist, 88(10): 1496-1513.**

604

605 Götze, J. et al., 1999. High-resolution cathodoluminescence combined with SHRIMP ion
606 probe measurements of detrital zircons. Mineralogical Magazine, 63(2): 179-187.

607 **Hanchar, J.M. and Miller, C.F., 1993. Zircon zonation patterns as revealed by**
608 **cathodoluminescence and backscattered electron images: Implications for**
609 **interpretation of complex crustal histories. Chemical Geology, 110(1-3): 1-13.**

610 **Hanchar, J.M. and Rudnick, R.L., 1995. Revealing hidden structures: The application**
611 **of cathodoluminescence and back-scattered electron imaging to dating zircons**
612 **from lower crustal xenoliths. Lithos, 36(3-4): 289-303.**

613 **Hazen, R.M. and Finger, L.W., 1979. Crystal structure and compressibility of zircon at**
614 **high pressure. American Mineralogist, 64: 196-201.**

615 **Hoskin, P.W.O., 2000. Patterns of chaos: Fractal statistics and the oscillatory chemistry**
616 **of zircon. Geochimica et Cosmochimica Acta, 64: 1905-1923.**

617 **Hoskin, P.W.O. and Black, L.P., 2000. Metamorphic zircon formation by solid-state**
618 **recrystallization of protolith igneous zircon. Journal of Metamorphic Geology,**
619 **18(4): 423-439.**

620 **Kempe, U., Gruner, T., Nasdala, L. and Wolf, D., 2000. Relevance of**
621 **cathodoluminescence for the interpretaton of U-Pb zircon ages, with an example**
622 **of an application to a study of zircons from the Saxonian Granulite Complex,**
623 **Germany. In: M. Pagel, V. Barbin, P. Blanc and D. Ohnenstetter (Editors),**
624 **Cathodoluminescence in Geosciences. Springer-Verlag, Berlin, pp. 415-455.**

625 **Kinny, P.D. and Friend, C.R.L., 1997. U-Pb isotopic evidence for the accretion of**
626 **different crustal blocks to form the Lewisian Complex of northwest Scotland.**
627 **Contributions to Mineralogy and Petrology, 129: 326-340.**

Koschek, G., 1993. Origin and Significance of the Sem Cathodoluminescence from Zircon. Journal of Microscopy, 171: 223-232.

Leroux, H., Reimold, W.U., Koeberl, C., Hornemann, U. and Doukhan, J.C., 1999. Experimental shock deformation in zircon: a transmission electron microscopic study. Earth and Planetary Science Letters, 169(3-4): 291-301.

Lloyd, G.E., Farmer, A.B. and Mainprice, D., 1997. Misoreintation analysis and the formation and orientation of subgrain and grain boundaries. Tectonophysics, 279: 55-78.

MacRae, C.M., Wilson, N.C., Johnson, S.A., Phillips, P.L. and Otsuki, M., 2005. Hyperspectral mapping - Combining cathodoluminescence and X-ray collection in an electron microprobe. Microscopy Research and Technique, 67(5): 271-277.

Murakami, T., Chakoumakos, B.C., Ewing, R.C., Lumpkin, G.R. and Weber, W.J., 1991. Alpha-decay event damage in zircon. American Mineralogist, 76(9-10): 1510-1532.

Nasdala, L., Götze, J., Hanchar, J.M., Gaft, M. and Krbetschek, M.R., 2004. Luminescence techniques in Earth sciences. In: A. Beran and E. Libowitzky (Editors), Spectroscopic Methods in Mineralogy. EMU Notes in Mineralogy. European Mineralogical Union, pp. 43-91.

Nasdala, L. et al., 2002. Annealing radiation damage and the recovery of cathodoluminescence. Chemical Geology, 191(1-3): 121-140.

Nasdala, L. et al., 2003. Spectroscopic methods applied to zircon. In: J.M. Hanchar and P.W.O. Hoskin (Editors), Reviews in Mineralogy and Geochemistry: Zircon. Reviews in Mineralogy and Geochemistry. Mineralogical Society of America, pp. 427-467.

Pagel, M., Barbin, V., Blanc, P. and Ohnenstetter, D., 2000. Cathodoluminescence in Geosciences: An Introduction. In: M. pagel, Barbin, V., Blanc, P., Ohnenstetter, D. (Editor), Cathodoluminescence in Geosciences. Springer, pp. 514.

Pidgeon, R.T., 1992. Recrystallization of oscillatory-zoned zircon: some geochronological and petrological implications. Contributions to Mineralogy and Petrology, 110: 463-472.

Prior, D.J., Wheeler, J., Peruzzo, L., Spiess, R. and Storey, C., 2002. Some garnet microstructures: an illustration of the potential of orientation maps and misorientation analysis in microstructural studies. Journal of Structural Geology, 24: 999-1011.

Reddy, S.M., Timms, N.E. and Eglington, B.M., 2008a. Electron backscatter diffraction analysis of zircon: A systematic assessment of match unit characteristics and pattern indexing optimization. American Mineralogist, 93: 187-197.

Reddy, S.M., Timms, N.E., Hamilton, P.J. and Smyth, H.R., 2008b. Deformation-related microstructures in magmatic zircon and implications for diffusion. Contributions to Mineralogy and Petrology, in press.

Reddy, S.M., Timms, N.E., Pantleon, W. and Trimby, T., 2007. Quantitative characterization of plastic deformation of zircon and geological implications. Contributions to Mineralogy and Petrology, 153: 625-645.

Reddy, S.M. et al., 2006. Crystal-plastic deformation of zircon: A defect in the assumption of chemical robustness. Geology, 34: 257-260.

Remond, G. et al., 1992. Cathodoluminescence Applied to the Microcharacterization of Mineral Materials - a Present Status in Experimentation and Interpretation. Scanning Microscopy, 6(1): 23-68.

Rimsa, A., Whitehouse, M.J., Johansson, L. and Piazolo, S., 2007. Brittle fracturing and fracture healing of zircon: An integrated cathodoluminescence, EBSD, U-Th-Pb, and REE study. American Mineralogist, 92(7): 1213-1224.

Rolland, Y., Cox, S., Boullier, A.-M., Pennacchioni, G. and Mancktelow, N., 2003. Rare earth and trace element mobility in mid-crustal shear zones: insights from the Mont Blanc Massif (Western Alps). Earth and Planetary Science Letters, 214(1-2): 203-219.

Smyth, H.R., Hamilton, P.J., Hall, R. and Kinny, P.D., 2007. The deep crust beneath island arcs: Inherited zircons reveal a Gondwana continental fragment beneath East Java, Indonesia. Earth and Planetary Science Letters, 258(1-2): 269-282.

Steyrer, H.P. and Sturm, R., 2002. Stability of zircon in a low-grade ultramylonite and its utility for chemical mass balancing: The shear zone at Miéville, Switzerland. Chemical Geology, 187(1-2): 1-19.

Timms, N., Kinny, P. and Reddy, S., 2006. Enhanced diffusion of Uranium and Thorium linked to crystal plasticity in zircon. Geochemical Transactions, 7(1): 10.

Vavra, G., 1990. On the kinematics of zircon growth and its petrogenetic significance: a cathodoluminescence study. Contributions to Mineralogy and Petrology, 106: 90-99.

Wheeler, J., Prior, D.J., Jiang, Z., Speiss, R. and Trimby, P.W., 2001. The petrological significance of misorientations between grains. Contributions to Mineralogy and Petrology, 141: 109-124.

Sample ID	Grain Length (μm)	Host rock	Location	Latitude/Longitude	U (ppm)	Th (ppm)	Age (Ma)
GST15[1, 2]	*ca.* 12,500	Sytectonic pyroxenite	Loch an Daimh Mór, Assynt Terrain, Lewisian complex, NW Scotland	58°19'54"N 05°07'57"W	20-60	30-110	$^{207}Pb/^{206}Pb$: 2451 ±14 (*35*)
IOZ[3, 4]	*ca.* 700	Deformed gabbro	ODP Leg 176, Atlantis II Ridge, Indian Ocean	32°43.392'S, 57°15.960'E	3-6	1-4	*ca.* 11
UX[5]	*ca.* 900	Metasomatised garnet websterite mantle xenolith	Udachnaya Kimberlite, Siberia	66°25'N 112°51'W	*c.* 12	*c.* 40	Proterozoic
Jhs2PON4[6, 7] grain 5	*ca.* 300	Undeformed porphyritic Andesite	Porongo district, E. Java	07°50'S 111°40'E	1297	408	$^{206}Pb/^{238}U$: 9.28 ± 0.21 (*20*)
Jhs2PON4[6, 7] grain 8	*ca.* 200				2112	810	

Table 2. Sample details. U-Pb ages are combined mean ages from multiple (*n*) SHRIMP analyses, e.g., Jhs2PON4 age is the weighted mean age from 20 analyses from 20 grains. Errors are 1σ. [1] Kinny & Friend (1997); [2] Timms et al. (2006); [3] Reddy et al. (2006); [4] Reddy et al. (2007); [5] Timms (unpublished data); [6] Smyth et al. (2007); [7] Reddy et al. (2008b).

CL activator		**Spectral peak positions**							
	Ref	~300nm	~400nm	~500nm	~600nm	~700nm	~800nm	~900nm	>900nm
Cr^{3+}	c				694	775			
Cr^{5+} (300 K)	c								1213
Cr^{5+} (12 K)	c								1132 1154 1191 1215 1258
Ce^{3+}	a	-	-	-	-	-	-	-	-
	b	355							
Pr^{3+}	a	Non-excited							
	b		489	596	621				
Nd^{3+}	a						809 874-**882**-892		
	b								
Sm^{3+}	a	342-**361**		559-570 597-**605**-565	615 646-661	702-710-725			
	b				601 612 647				
Eu^{3+}	a	302-363-386		560 **595**-616-632	652-656	692-**704**			
	b			596	616 654	702 707			
Gd^{3+}	a	30-360 308-**313**							
	b	312							
Tb^{3+}	a	**382**	415 436 459 475	489 **548** 588-596	624 666 672 685	766	837 878		
	b	383	415 437 489	548					
Dy^{3+}	a	(280) 362	456 **483**	542 **578**	609 646-666	754 780	810-828-845-861		
	b		478	575					
Ho^{3+}	a	-	-	-	-	-	-	-	
	b			549	665				
Er^{3+}	a	323	**405 474**	530	619				
	b			549 559					
Tm^{3+}	a	291 **350**-**364**	383 454 481	513	656-679	758	790-805		
	b	289 347	458 483						
Intrinsic	d	(300)-340-(380)							
Intrinsic	d	(210)-285-(340)							
Intrinsic	e			(500-700)					
Intrinsic	f		(<300-475)						
Intrinsic	e			(490-700)					
Intrinsic	g								
Intrinsic	h			(400)-430-580-(800)					

Table 1. Spectral peak positions for cathodoluminescence due to REEs, other trace elements, and intrinsic sources in zircon. Approximate spectral range of intrinsic broadband emission indicated by parentheses. Dominant peaks are indicated in bold. a (Blanc, 2000); b (Gaft et al., 2000b); c (Gaft et al., 2000a); d (Nasdala et al., 2002); e (Nasdala et al., 2003); f (Hanchar and Rudnick, 1995); g (Timms et al., 2006); h (Götze et al., 1999).

EBSD map settings and statistics	**Fig 1 IOZ**	**Fig. 2 GST15**	**Fig. 4 UX**	**Fig. 5 Jhs2PON4-5**	**Fig. 6 Jhs2PON4-8**
EBSP collection time per frame (ms)	60	60	60	60	60
Background (frames)	64	64	64	64	64
EBSP noise reduction (frames)	4	4	4	4	4
(binning)	4x4	2x2	2x2	4x4	4x4
(gain)	Low	High	Low	Low	Low
Number of reflectors	50	80	80	80	80
Hough resolution	60	65	65	65	65
Match units	HKL b.i.f.	Zircon [2]*	HKL b.i.f.	Zircon [3]*	Zircon [3]*
Band detection – min/max no. of bands	6/10	6/8	6/8	6/8	6/8
Mean angular deviation cut off	1.6	1.3	1.3	1.3	1.3
Step size (µm)	1	1.5	1	1	1
Step X	172	340	392	180	276
Step Y	123	340	428	390	190
Average mean angular deviation (°)	0.3702	0.4955	0.5201	0.4216	0.5107
EBSD noise reduction					
Wildspike removal (% of total data)	0.00006	0.032	0.176	0.058	0.264
5 neighbour zero solution extrapolation (% of total data)	0.17	14.65	16.67	4.96	14.99
Orientation averaging filter** (Filter size / smoothing angle / artefact angle)	3x3 / 5˚ / 1˚	3x3 / 5˚ / 1˚	3x3 / 5˚ / 1˚	3x3 / 5˚ / 1˚	3x3 / 5˚ / 1˚
Wavelength CL map settings					
Dwell time per point (ms)	50	50	25	25	25
Step size (µm)	0.5	2	1	1	1
Step X	200	250	440	300	330
Step Y	250	250	440	500	230

Table 3. Settings for EBSD and wavelength CL maps. *generated from structure file cards in the Mincryst crystallographic database. ** after Humphreys et al. (2001).

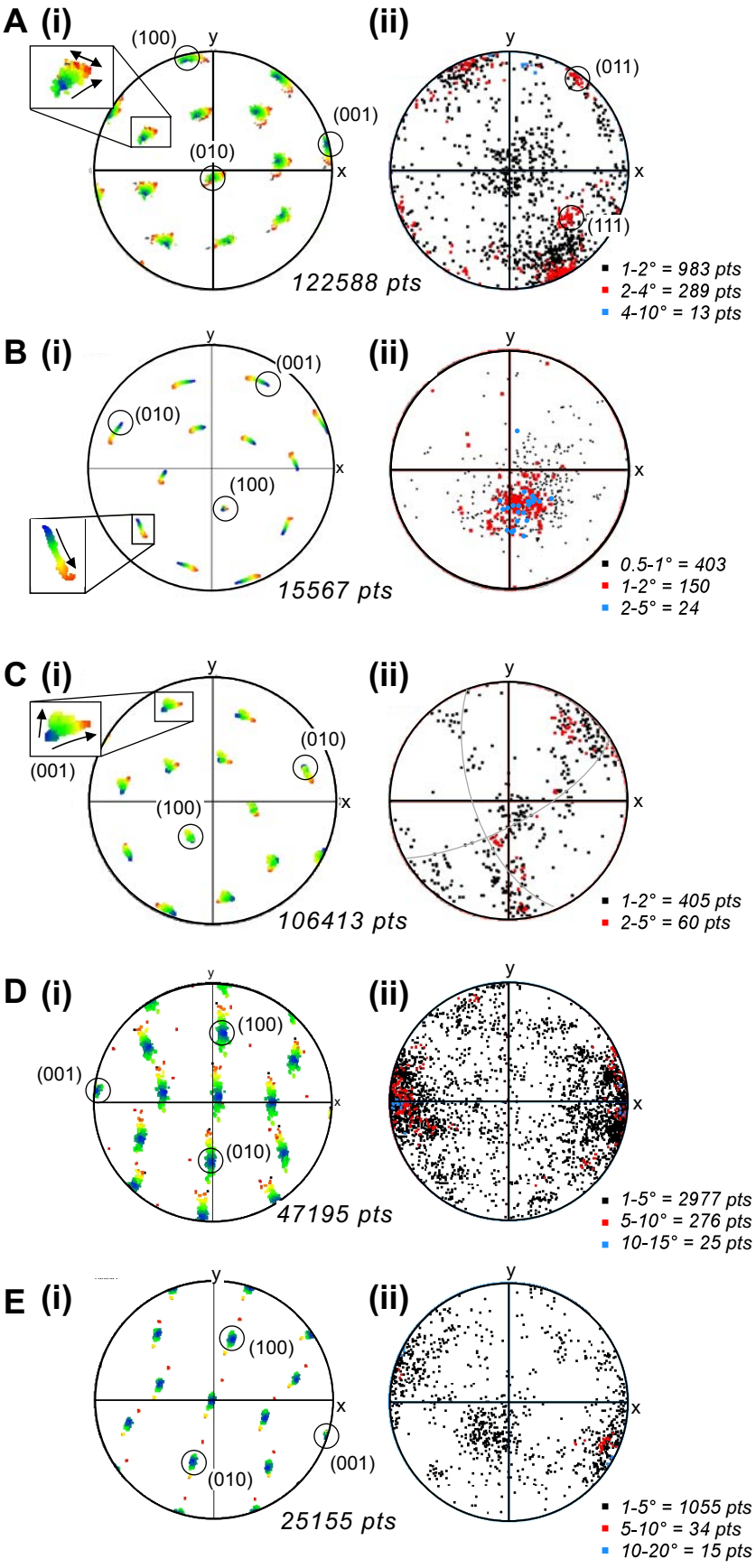

Timms & Reddy Figure 8

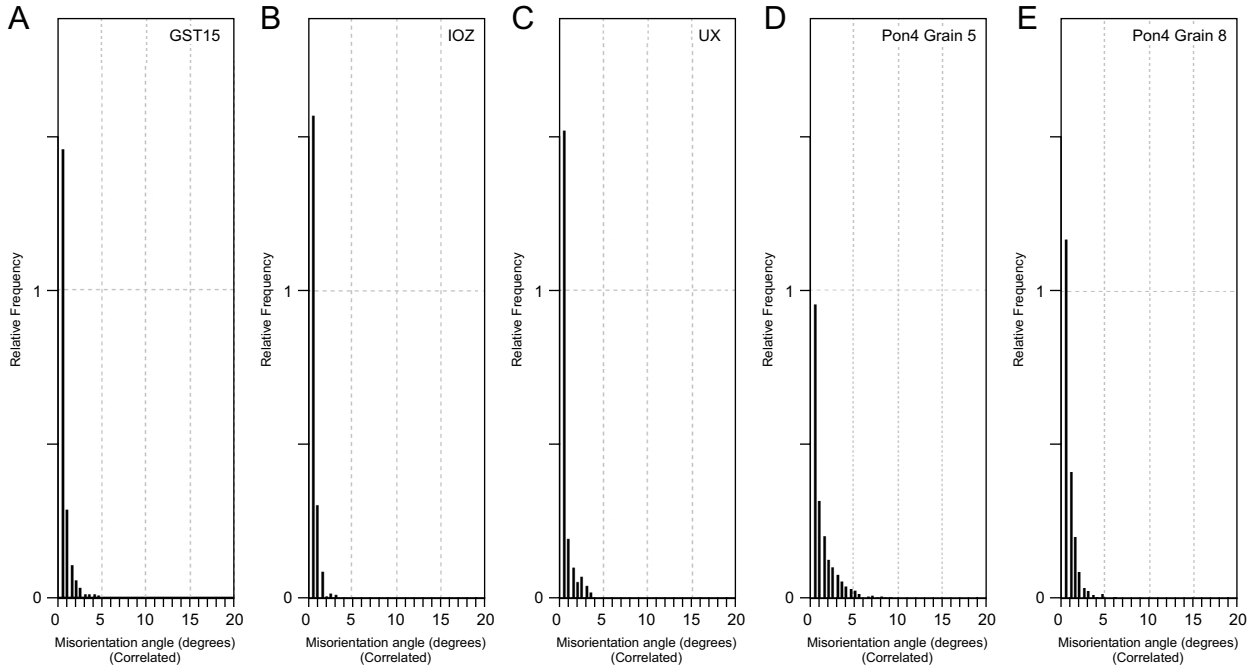

Timms & Reddy Figure 7

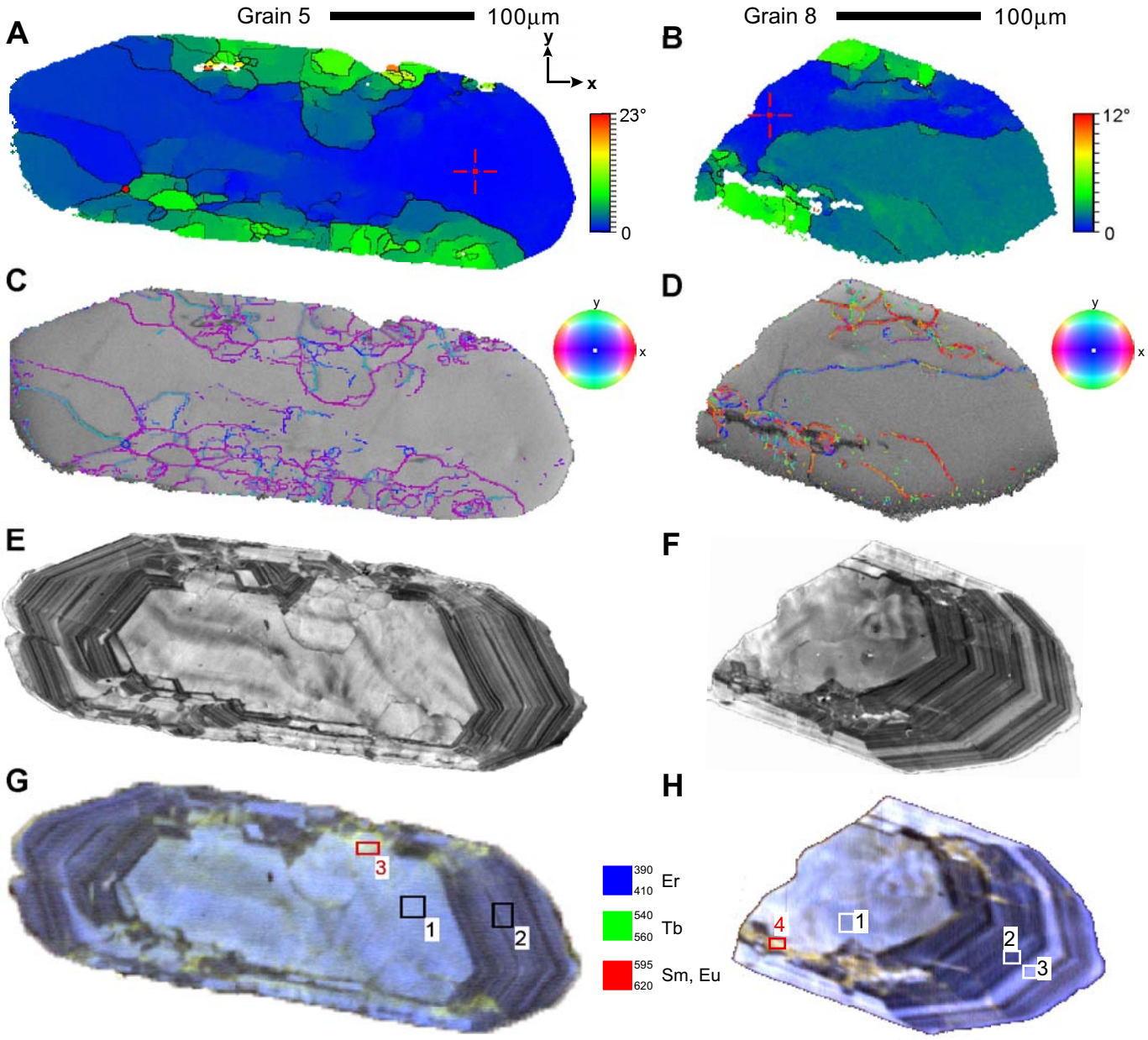

Timms & Reddy Figure 6

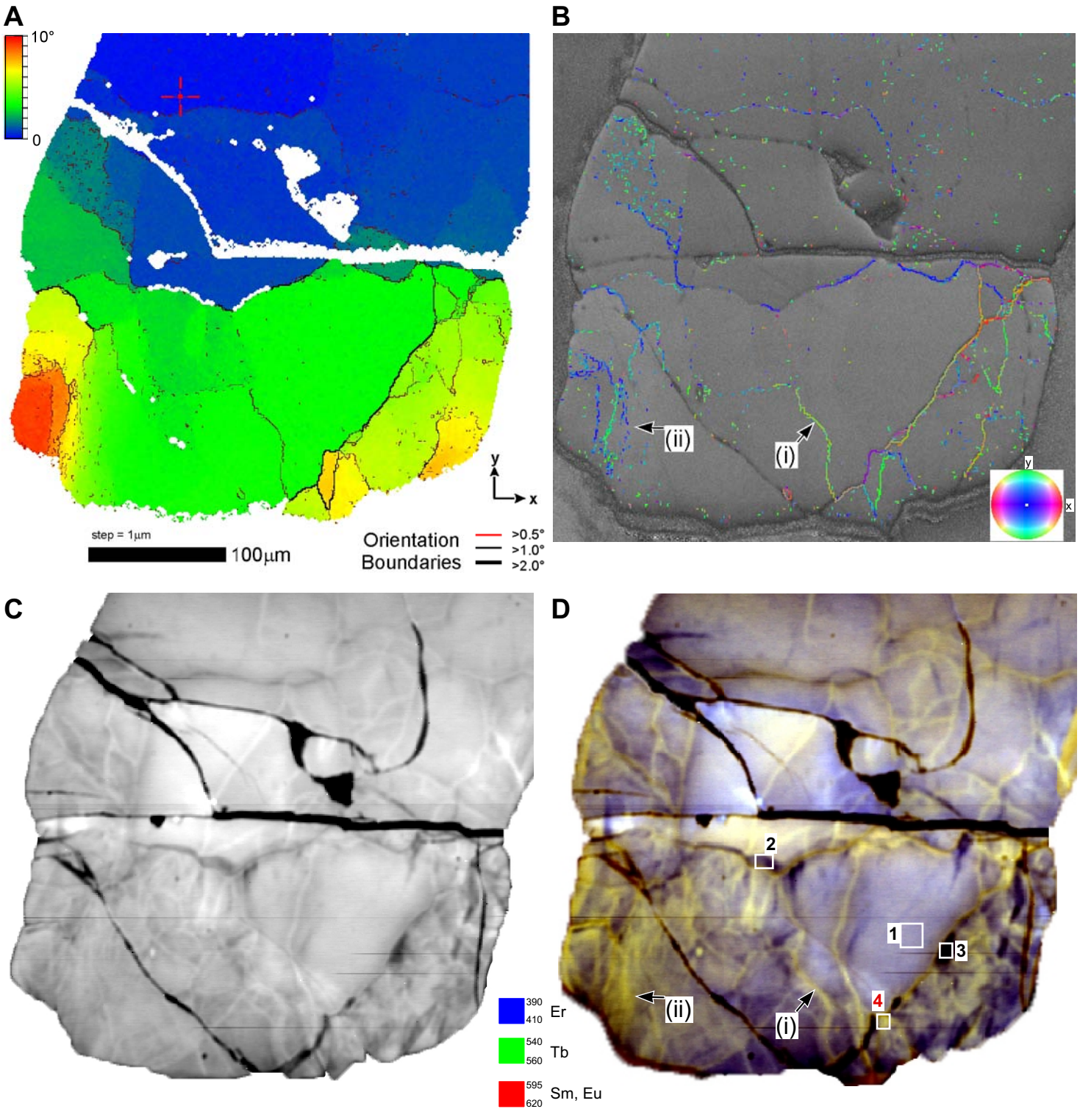

Timms & Reddy Figure 5

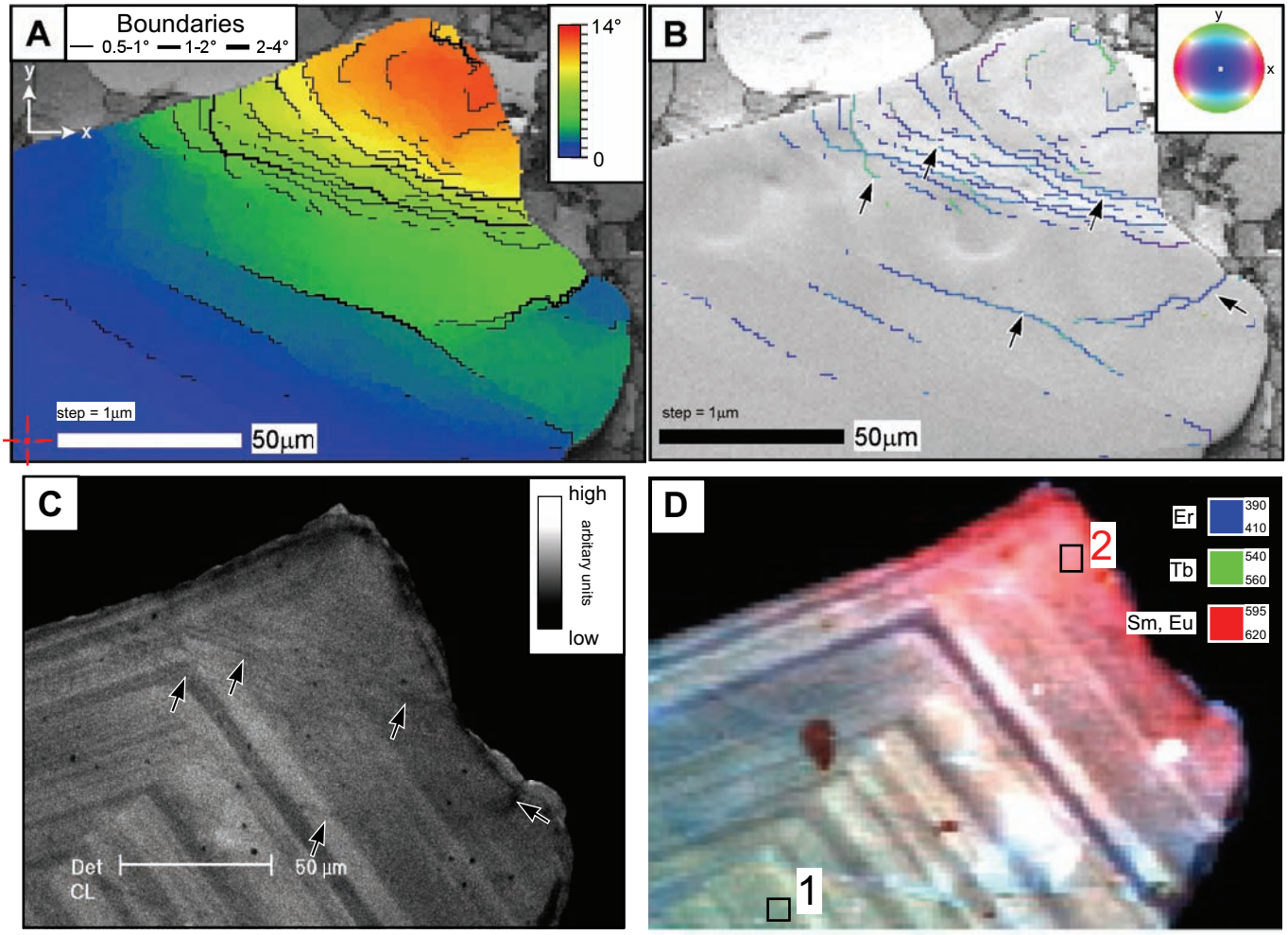

Timms & Reddy Figure 4

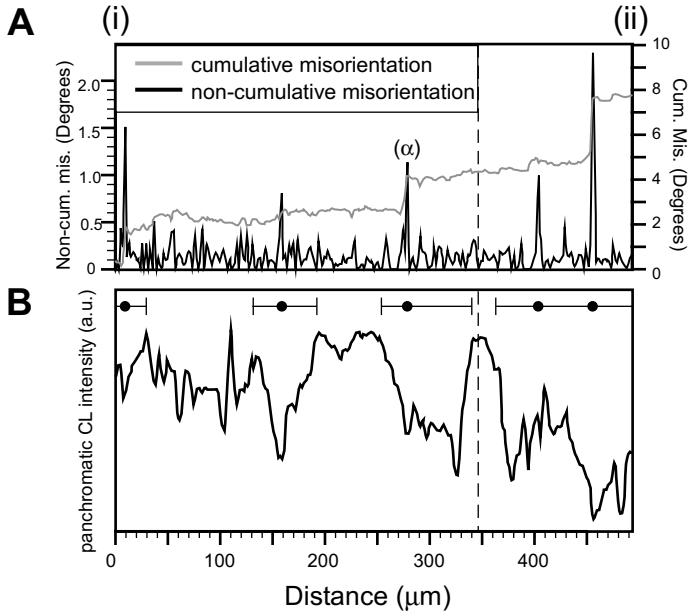

Timms & Reddy Figure 3

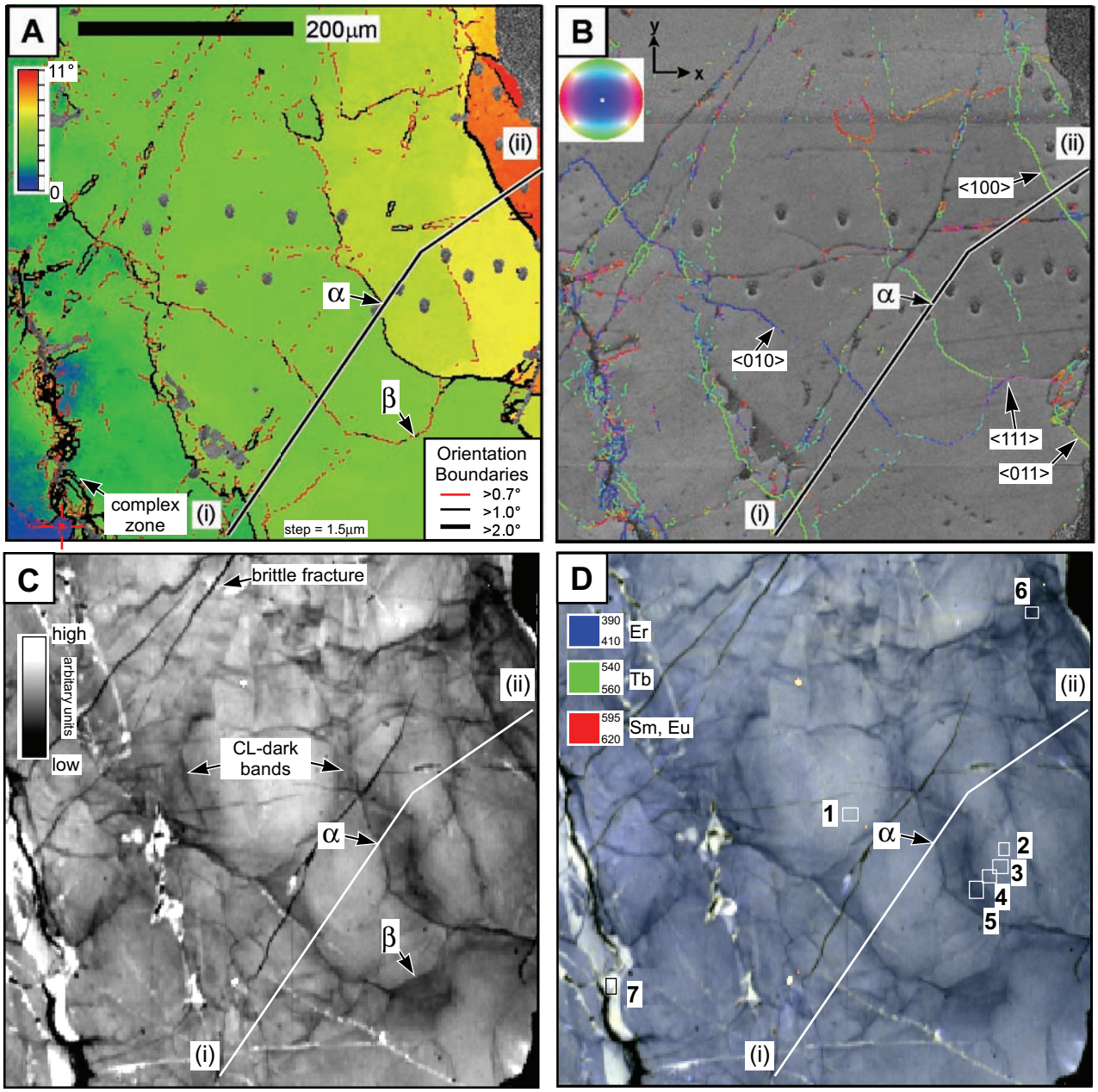

Timms & Reddy Figure 2

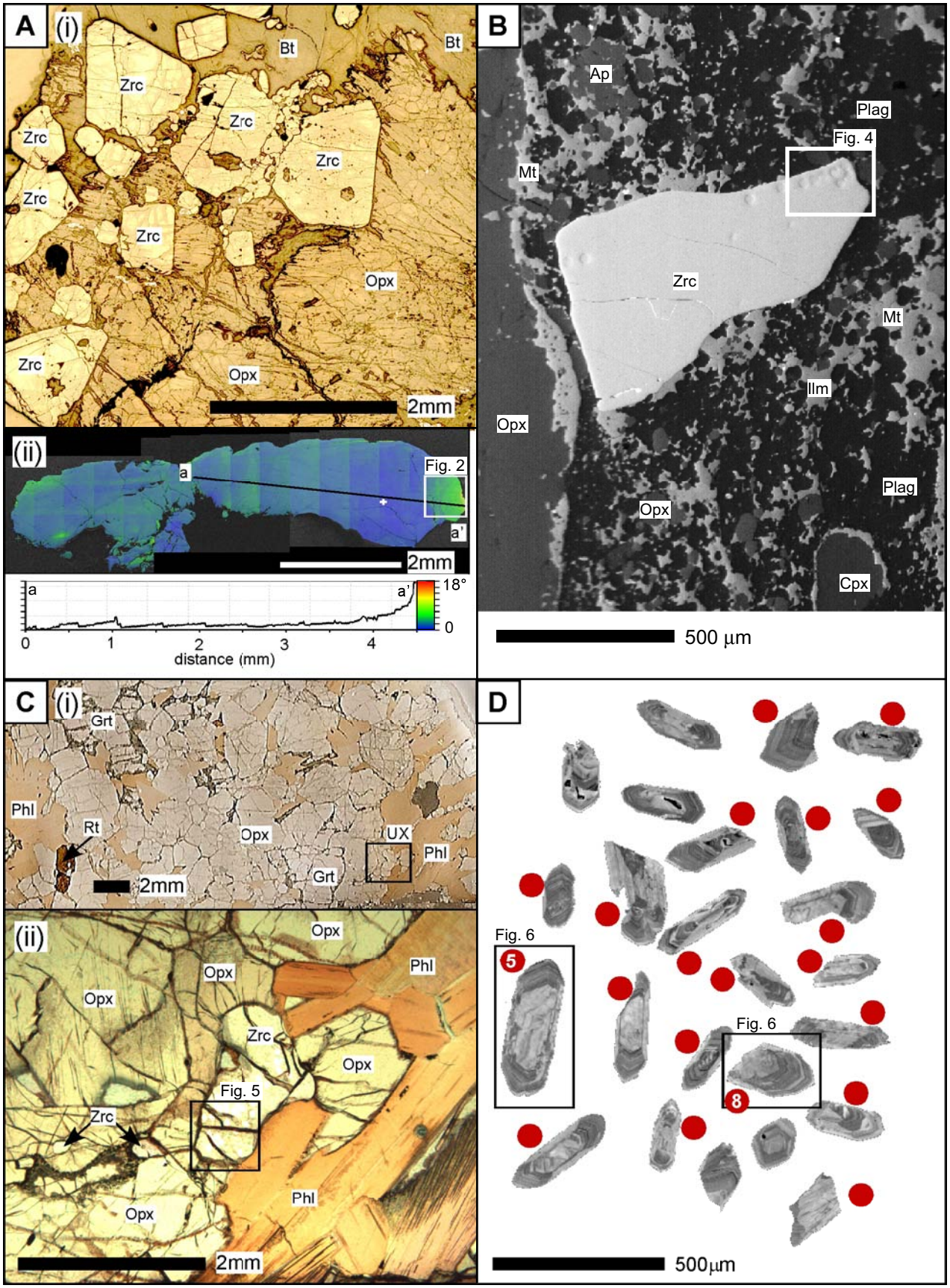

Timms & Reddy Figure 1

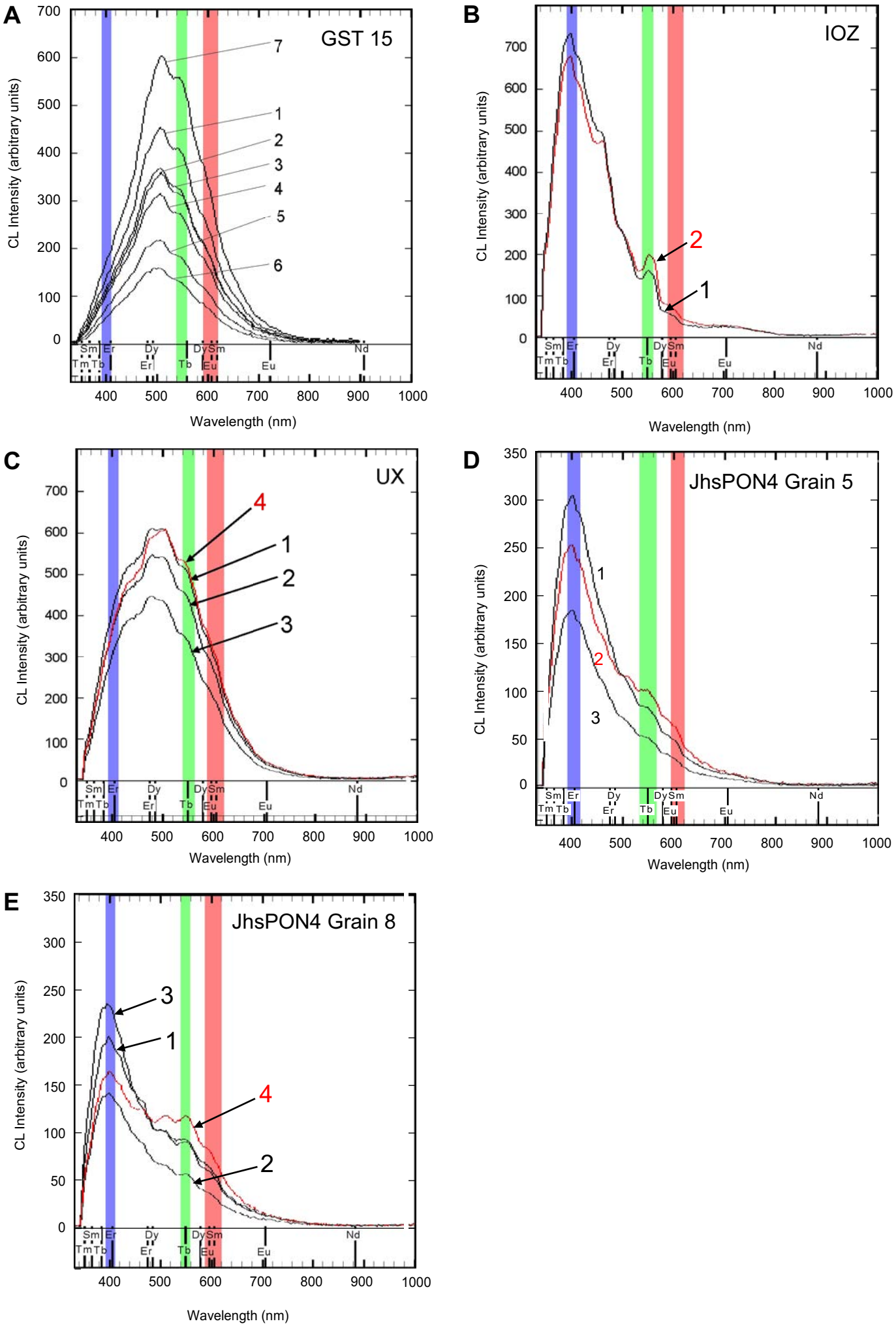

Timms & Reddy Figure 9